THE WEAKLY NONLINEAR SATURATION OF THE MAGNETOROTATIONAL INSTABILITY

Clark, S.E.[1], Oishi, J.S. [2,3], and Mac Low, M.-M.[1,2]

Draft version November 21, 2014

ABSTRACT

The magnetorotational instability (MRI) is a fundamental process of accretion disk physics, but its saturation mechanism remains poorly understood. We present an analytic analysis of the nonideal MRI in the weakly nonlinear regime – that is, when the MRI system is just unstable to its most unstable mode.

1. INTRODUCTION

For matter to accrete from a disk onto a central object, angular momentum must be transported radially outward in the disk. The transport mechanism is likely turbulent (Shakura & Sunyaev 1973). Since its discovery by Chandrasekhar (1960) and subsequent rediscovery by Balbus & Hawley (1991), the MRI remains the leading explanation for rapid angular momentum transport in astrophysical disks. The instability arises when a differentially rotating disk is threaded by a vertical magnetic field. The presence of the magnetic field destabilizes the disk gas, driving turbulence and angular momentum transport.

The MRI evolves via a period of linear growth, followed by nonlinear saturation. The nonlinear evolution of the MRI is a complex process, and an understanding of the mechanism by which the MRI saturates remains elusive. Most previous works on MRI saturation have studied the problem in simulation. Indeed, only a few works have tackled MRI saturation analytically. Knobloch & Julien (2005) analyze the MRI in the strongly nonlinear regime, by following the already-developed MRI modes into asymptotic saturation. They find that this saturation proceeds via modification of the background shear. Another notable analytic work is that of Pessah (2010), who presents an analysis of MRI saturation via secondary instabilities. This work suggests that MRI saturation can be caused by parasitic instabilities growing off of the primary MRI modes, in particular by Kelvin-Helmholtz and tearing mode instabilities, depending on parameter regime.

This work builds on the investigations of Umurhan et al. (2007b; see also Umurhan et al. 2007a), who first conducted an analytic analysis of the MRI in the weakly nonlinear regime. The present work adds to this foundation both in subject, with our additional analysis of the helical MRI, as well as in scope, with a detailed analysis of MRI saturation properties across parameter space. In particular, we attempt to elucidate the role of boundary layers in the saturation of the MRI, as this is of fundamental importance to laboratory MRI work.

We develop this investigation with the goal of providing a rigorous analytical framework that will be used to make predictions for laboratory MRI experiments. Observing MRI in a laboratory setting would open a new avenue for studying MRI dynamics and saturation. In recent years much experimental progress has been made, although no experiment has yet yielded a confirmed detection. Of most immediate interest to this work is the Princeton Plasma Physics Laboratory (PPPL) MRI experiment, which has a design roughly analogous to the set-up investigated here (see §2 for further details). The Madison plasma dynamo experiment is a multi-purpose plasma device which may be a vehicle for MRI studies in the near future (Cooper et al. 2014). The helical MRI, an instability related to the standard MRI but easier to excite in the laboratory, is the focus of the Potsdam Rossendorf Magnetic Instability Experiment (PROMISE) in Dresden. PROMISE has already detected helical MRI in the laboratory (e.g. Stefani et al. 2006), and we discuss possible applications of our framework to the helical MRI in §5. A spherical Couette experiment claimed to have detected MRI in 2004 (Sisan et al.), but most likely detected unrelated MHD instabilities instead (Hollerbach 2009; Gissinger et al. 2011).

The focus of this work is the weakly nonlinear regime of the MRI. This is where the initial linear growth phase of the instability begins to give way to nonlinear saturation. Weakly nonlinear analysis is the perturbation analysis of a system that is just unstable to its most unstable mode. The system in its marginal state, when the most unstable mode neither grows nor decays, is tuned slightly into instability. This excites a band of wavemodes around the most unstable mode, which interact nonlinearly. In order to track the evolution of the system on both rapid and slow scales, we conduct a formal multiscale analysis. We develop and solve this framework in §3, conduct a full parameter space study in §4, and explore the implications of our findings in §5.

2. SET-UP

We analyze a magnetized Taylor Couette flow, representing a differentially rotating, conducting fluid between two cylinders which are driven at different speeds. We initialize an angular velocity profile which decreases outward from the axis of rotation, and a weak vertical magnetic field. These are the only two conditions required to excite MRI. The differential rotation profile is

$$\Omega\left(r\right) \propto \Omega_0 \left(\frac{r}{r_0}\right)^{-q}, \qquad (1)$$

[1] Department of Astronomy, Columbia University, New York, NY
[2] Department of Astrophysics, American Museum of Natural History, New York, NY
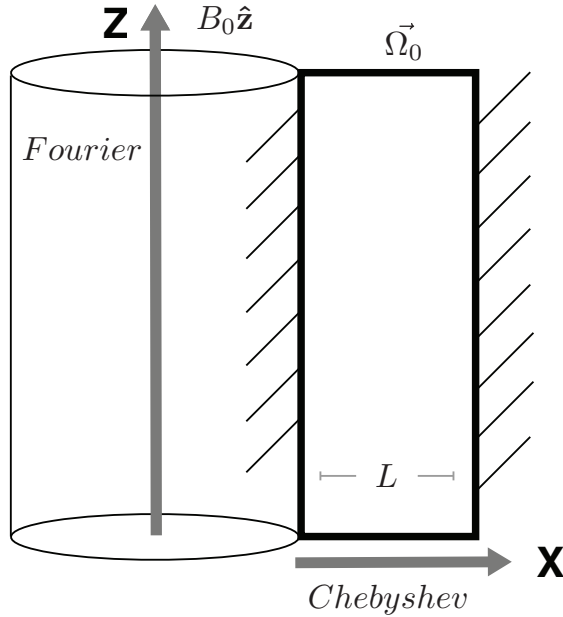[3] Department of Physics, SUNY Farmingdale

FIG. 1.— Schematic diagram of our set-up, an axisymmetric magnetized Taylor Couette flow. We investigate a 2D slice of the X-Z (radial-vertical) plane. Our domain is represented by the bolded black box, of width L. The radial dimension is solved with a basis of Chebyshev polynomials, and the vertical dimension is solved on a Fourier basis (see §5.)

where q, the shear parameter, is $3/2$ for Keplerian rotation. The initial background magnetic field is

$$\mathbf{B} = B_0 \hat{z}, \tag{2}$$

a constant, vertical field.

We analyze this system in the thin-gap regime, where the channel is radially narrow. Formally, this means

$$(R_2 - R_1) \ll \frac{1}{2}(R_2 + R_1), \tag{3}$$

where R_1 is the radius of the inner cylinder and R_2 is the radius of the outer cylinder, such that the width of the channel is small compared to its distance from the center of rotation. The imposition of the thin-gap approximation eliminates channel modes, the axisymmetric MRI modes that are exact solutions of the incompressible MRI in the shearing box approximation (Goodman & Xu 1994). Implications of this approximation are discussed further in §5.

Our domain is designed to be relevant to the apparatus of the PPPL MRI experiment (see §5 for further discussion). We use periodic vertical boundary conditions. On the radial boundaries of our domain – the inner and outer cylinders – we apply no-slip, perfectly conducting boundary conditions. The choice of boundary conditions dictates the functional bases on which our system is spectrally solved. This is explained further in §3. A diagram of our set-up is shown in Figure 1.

3. WEAKLY NONLINEAR ANALYSIS

We perform a weakly nonlinear analysis following the lead of Umurhan et al., and use much of the same nota-

tion, with some changes for added clarity.

We solve the equations of non-ideal, axisymmetric, incompressible magnetized Taylor Couette flow. We solve the momentum equation,

$$\partial_t \mathbf{u} + \mathbf{u} \cdot \nabla \mathbf{u} = -\frac{1}{\rho}\nabla P - \nabla \Phi + \frac{1}{\rho}(\mathbf{J} \times \mathbf{B})$$
$$+ \nu \nabla^2 \mathbf{u} - 2\mathbf{\Omega} \times \mathbf{u} - \mathbf{\Omega} \times (\mathbf{\Omega} \times \mathbf{r}), \tag{4}$$

and the induction equation,

$$\partial_t \mathbf{B} = \nabla \times (\mathbf{u} \times \mathbf{B}) + \eta \nabla^2 \mathbf{B}. \tag{5}$$

In the above, P is the gas pressure, ν is the kinematic viscosity, η is the microscopic diffusivity, $\nabla \Phi$ is the gravitational force per unit mass, and the current density is

$$\mathbf{J} = \frac{2}{\beta}\nabla \times \mathbf{B}. \tag{6}$$

Equations 4 and 5 are subject to the magnetic solenoid and incompressibility constraints,

$$\nabla \cdot \mathbf{B} = 0 \tag{7}$$

and

$$\nabla \cdot \mathbf{u} = 0. \tag{8}$$

We axisymmetrically perturb all three vector components of each of the fluid quantities. We nondimensionalize the equations, with lengths nondimensionalized by L, velocities by $\Omega_0 L$, magnetic fields by B_0, and pressure by $\Omega_0^2 L^2 \rho_0$, where L is the channel width, Ω_0 is the rotation rate at the center of the channel, and ρ_0 is the constant pressure in the base state (see Figure 1). We define the nondimensional Reynolds number,

$$\mathrm{Re} \equiv \frac{\Omega_0 L^2}{\nu}, \tag{9}$$

and magnetic Reynolds number,

$$\mathrm{Rm} \equiv \frac{\Omega_0 L^2}{\eta}. \tag{10}$$

We also define a plasma beta parameter,

$$\beta \equiv \frac{\Omega_0^2 r_0^2}{v_A^2}, \tag{11}$$

where the Alfvén sped v_A is

$$v_A^2 = \frac{B_0^2}{\rho_0}. \tag{12}$$

The fluid symbols $\mathbf{u}$, $\mathbf{B}$, etc. will henceforth be used to refer to the nondimensional, perturbed quantities.

We define the flux function A and streamfunction Ψ. A is the familiar two-dimensional vector potential. A and Ψ are scalar fields. The curl of A and the curl of Ψ are defined as the magnetic field and velocity, respectively, and so A and Ψ automatically satisfy our constraints.

A is thus related to the magnetic field as

$$\mathbf{B} = \begin{bmatrix} \partial_z A \\ B_y \\ -\partial_x A \end{bmatrix}, \tag{13}$$

and $\boldsymbol{\Psi}$ is defined analogously.

Our final equation set is

$$\partial_t \nabla^2 \Psi + J\left(\Psi, \nabla^2 \Psi\right) - 2\partial_z u_y =$$
$$\frac{2}{\beta} B_0 \partial_z \nabla^2 A + \frac{2}{\beta} J\left(A, \nabla^2 A\right) + \frac{1}{\mathrm{Re}} \nabla^4 \Psi \quad (14)$$

$$\partial_t u_{1y} + J\left(\Psi, u_y\right) + (2-q)\,\Omega_0 \partial_z \Psi =$$
$$\frac{2}{\beta} B_0 \partial_z B_y + \frac{2}{\beta} J\left(A, B_y\right) + \frac{1}{\mathrm{Re}} \nabla^2 u_y \quad (15)$$

$$\partial_t A \quad = \quad B_0 \partial_z \Psi \;+\; J\left(A, \Psi\right) \;+\; \frac{1}{\mathrm{Rm}} \nabla^2 A \quad (16)$$

$$\partial_t B_y = B_0 \partial_z u_y + J\left(A, u_y\right) - J\left(\Psi, B_y\right)$$
$$+ \frac{1}{\mathrm{Rm}} \nabla^2 B_y - q\Omega_0 \partial_z A, \quad (17)$$

where J is the Jacobian operator,

$$J\left(f, g\right) \equiv \partial_z f \partial_x g - \partial_x f \partial_z g. \quad (18)$$

Note that working in terms of the flux function raises the order of the first momentum equation.

The weakly nonlinear regime is where the MRI system is nonlinearly unstable to only the most unstable mode of the linear solution. We find the marginal state, where the most unstable linear MRI mode neither grows nor decays, for a given set of dimensionless parameters.

B_0 appears in Equations 14 - 17 because it is the nondimensionalized background field strength. Because we nondimensionalize B by the magnitude of the background field strength, $B_0 \equiv 1$. In order to study our system in the weakly nonlinear regime, we tune the background magnetic field down away from stability (recall that stronger vertical fields stabilize the MRI). We do so by substituting $B = B_0\left(1 - \epsilon^2\right)$. The degree of departure from the marginal state is measured by the small parameter ϵ. An $\mathcal{O}\left(\epsilon^2\right)$ weakening of the background magnetic field destabilizes a band of wave modes with width of $\mathcal{O}\left(\epsilon\right)$, which interact nonlinearly.

The destabilizing substitution is made, and Equations 14 - 17 are rewritten such that the fluid variables are contained in a state vector $\mathbf{V} = \left[\Psi, u_y, A, B_y\right]^{\mathrm{T}}$. This yields the system of equations

$$\mathcal{D}\partial_t \mathbf{V} + \mathbf{N} = \mathcal{L}\mathbf{V} - \epsilon^2 \partial_z \mathcal{X}\mathbf{V} - \epsilon^2 \partial_z^3 \mathcal{L}_3 \mathbf{V}, \quad (19)$$

where $\mathcal{L} \equiv \mathcal{L}_0 + \mathcal{L}_1 \partial_z + \mathcal{L}_2 \partial_z^2 + \mathcal{L}_3 \partial_z^3 + \mathcal{L}_4 \partial_z^4$,

and

$$\mathcal{D} = \begin{bmatrix} \nabla^2 & 0 & 0 & 0 \\ 0 & 1 & 0 & 0 \\ 0 & 0 & 1 & 0 \\ 0 & 0 & 0 & 1 \end{bmatrix} \quad (20)$$

$$\mathcal{L}_0 = \begin{bmatrix} \frac{1}{\mathrm{Re}}\partial_x^4 & 0 & 0 & 0 \\ 0 & \frac{1}{\mathrm{Re}}\partial_x^2 & 0 & 0 \\ 0 & 0 & \frac{1}{\mathrm{Rm}}\partial_x^2 & 0 \\ 0 & 0 & 0 & \frac{1}{\mathrm{Rm}}\partial_x^2 \end{bmatrix} \quad (21)$$

$$\mathcal{L}_1 = \begin{bmatrix} 0 & 2 & \frac{2}{\beta}\partial_x^2 & 0 \\ (\Omega_0 - 2)q & 0 & 0 & \frac{2}{\beta} \\ 1 & 0 & 0 & 0 \\ 0 & 1 & -q\Omega_0 & 0 \end{bmatrix} \quad (22)$$

$$\mathcal{L}_2 = \begin{bmatrix} 2\frac{1}{\mathrm{Re}}\partial_x^2 & 0 & 0 & 0 \\ 0 & \frac{1}{\mathrm{Re}} & 0 & 0 \\ 0 & 0 & \frac{1}{\mathrm{Rm}} & 0 \\ 0 & 0 & 0 & \frac{1}{\mathrm{Rm}} \end{bmatrix} \quad (23)$$

$$\mathcal{L}_3 = \begin{bmatrix} 0 & 0 & \frac{2}{\beta} & 0 \\ 0 & 0 & 0 & 0 \\ 0 & 0 & 0 & 0 \\ 0 & 0 & 0 & 0 \end{bmatrix} \quad (24)$$

$$\mathcal{L}_4 = \begin{bmatrix} \frac{1}{\mathrm{Re}} & 0 & 0 & 0 \\ 0 & 0 & 0 & 0 \\ 0 & 0 & 0 & 0 \\ 0 & 0 & 0 & 0 \end{bmatrix} \quad (25)$$

$$\mathcal{X} = \begin{bmatrix} 0 & 0 & \frac{2}{\beta}\partial_x^2 & 0 \\ 0 & 0 & 0 & \frac{2}{\beta} \\ 1 & 0 & 0 & 0 \\ 0 & 1 & 0 & 0 \end{bmatrix}. \quad (26)$$

The nonlinear terms are contained in a vector $\mathbf{N} = \left[N^{(\Psi)}, N^{(u_y)}, N^{(A)}, N^{(B_y)}\right]^{\mathrm{T}}$, where

$$\mathbf{N} = \begin{bmatrix} J(\Psi, \nabla^2 \Psi) - \frac{2}{\beta} J(A, \nabla^2 A) \\ J(\Psi, u_y) - \frac{2}{\beta} J(A, B_y) \\ -J(A, \Psi) \\ J(\Psi, B_y) - J(A, u_y) \end{bmatrix}. \quad (27)$$

We conduct a formal multiscale analysis. Our perturbations are characterized in terms of fast and slow-moving variables, in order to simultaneously track their evolution on fast and slow scales. The relative scalings of the fast and slow scales are determined as follows. When our four equations are linearized for axisymmetric perturbations of the form $e^{\sigma t + ik_x x + ik_z z}$, we can derive the linear dispersion relation, which is fourth order in σ (Appendix A). The fast and slow variables are then defined such that each of the temporal and spatial eigenvalues appear at the same lowest order in the linear dispersion relation. The scalings are

$$X \equiv \epsilon x, \; Y \equiv \epsilon y, \; Z \equiv \epsilon z, \; T \equiv \epsilon^2 t. \quad (28)$$

See Figure 2. Note that these are the same scalings as apply to Rayleigh-Bénard convection and hydrodynamic Taylor Couette flow. In analogy to these problems, we posit slow variation in both Z and T. Each operator is expanded to reflect these scalings – for instance, ∂_z becomes $\partial_z + \epsilon \partial_Z$.
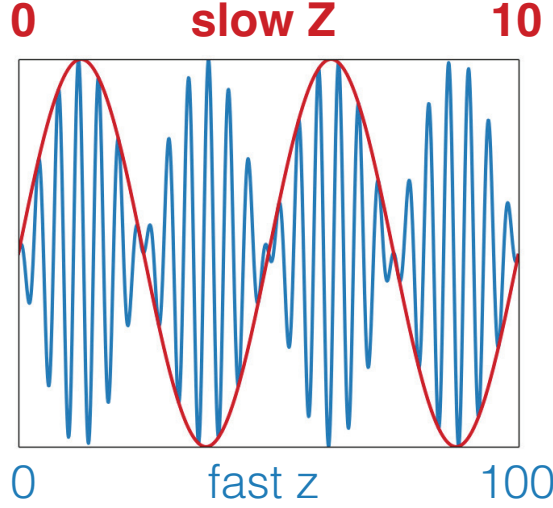
FIG. 2.— Cartoon illustrating fast and slow-moving variables (Equation 28).

The multiple scale dependencies of our solution are encoded into an ansatz for the linear MRI solution at marginality,

$$\mathbf{V_1} = \alpha(T, Z)\mathbb{V}_{11}(x)e^{ik_c z} + c.c. + \beta(T, Z)\mathbb{U}_{11}(x) \quad (29)$$

where α is a slowly-varying amplitude equation and c.c. denotes the complex conjugate. The x dependence is contained in $\mathbb{V}_{11} = (\Psi_{11}, u_{11}, A_{11}, B_{11})^{\mathbf{T}}$, and must be solved subject to the radial boundary conditions. The periodic vertical boundary conditions allow us to posit the z dependence, where k_c is the value of the vertical wavenumber at marginality. As noted by Umurhan et al., there exists a spatially constant neutral mode solution to the B_y equation, with $\mathbb{U}_{11} = (0, 0, 0, 1)^{\mathbf{T}}$. The slowly-varying amplitude β encodes the slow evolution of this mode.

Because we investigate the system at marginality, where the growth rate $\sigma = 0$, the ∂_t terms drop out. Thus after the multiscale expansion our system becomes

$$\epsilon^2 \mathcal{D}\partial_T \mathbf{V} + \mathbf{N} = \mathcal{L}\mathbf{V} + \epsilon\widetilde{\mathcal{L}}_1\partial_Z\mathbf{V} + \epsilon^2\widetilde{\mathcal{L}}_2\partial_Z^2\mathbf{V}$$
$$- \epsilon^2\partial_z\mathcal{X}\mathbf{V} - \epsilon^2\partial_z^3\mathcal{L}_3\mathbf{V} + \mathcal{O}(\epsilon^3), \quad (30)$$

where

$$\widetilde{\mathcal{L}}_1 = \mathcal{L}_1 + 2\mathcal{L}_2\partial_z + 3\mathcal{L}_3\partial_z^2 + 4\mathcal{L}_4\partial_z^3 \quad (31)$$

and

$$\widetilde{\mathcal{L}}_2 = \mathcal{L}_2 + 3\mathcal{L}_3\partial_z + 6\mathcal{L}_4\partial_z^2. \quad (32)$$

The state vector is expanded in a perturbation series in orders of ϵ,

$$\mathbf{V} = \epsilon\mathbf{V_1} + \epsilon^2\mathbf{V_2} + \epsilon^3\mathbf{V_3} + ... \quad (33)$$

The multiscale expansion of the operators and the perturbation series expansion of the fluid quantities com-

bine to make the expansion of the nonlinear vector $\mathbf{N}$ formidable, and we relegate the expansion to Appendix B. $\mathbf{N}$ becomes

$$\mathbf{N} = \epsilon^2\mathbf{N_2} + \epsilon^3\mathbf{N_3} + \mathcal{O}(\epsilon^4). \quad (34)$$

Substituting Equation 33 into Equation 30 yields the perturbed, expanded equations. We solve these successively in increasing orders of ϵ.

To $\mathcal{O}(\epsilon)$, we have

$$\mathcal{L}\mathbf{V_1} = 0. \quad (35)$$

To $\mathcal{O}(\epsilon^2)$,

$$\mathcal{L}\mathbf{V_2} = \mathbf{N_2} - \widetilde{\mathcal{L}}_1\partial_Z\mathbf{V_1}. \quad (36)$$

To $\mathcal{O}(\epsilon^3)$,

$$\mathcal{D}\partial_T\mathbf{V_1} + \mathbf{N_3} = \mathcal{L}\mathbf{V_3} + \widetilde{\mathcal{L}}_1\partial_Z\mathbf{V_2} + \widetilde{\mathcal{L}}_2\partial_Z^2\mathbf{V_1}$$
$$- \partial_Z\mathcal{X}\mathbf{V_1} - \partial_z^3\mathcal{L}_3\mathbf{V_1}. \quad (37)$$

In the above, we find that $\mathbf{V_2}$ takes the form

$$\mathbf{V_2} = \alpha^2 e^{i2Qz}\mathbb{V}_{22}(x) + |\alpha|^2\,\mathbb{V}_{20}(x)$$
$$- \partial_Z\alpha\mathbb{V}_{21}(x)e^{iQz} - \partial_Z\beta\mathbb{U}_{20}(x) + c.c. \quad (38)$$

The $\mathcal{O}(\epsilon)$ equation is the equation for the linear MRI at marginality. This is the equation that is solved to find the $\mathbb{V}_{11}$ component of Equation 29.

The partial differential equations that comprise Equations 35 to 37 are solved in succession subject to no-slip, perfectly conducting radial boundary conditions, defined as

$$\Psi = \partial_x\Psi = u_y = A = \partial_x B_y = 0. \quad (39)$$

The practical advantage of our ansatz construction (Equation 29) is clear: the separable x-dependence means that the radial boundary conditions are solved in only one dimension. Thus our analytical framework is able to side-step many of the resolution issues faced by multidimensional simulations. We are able to resolve even small-scale structure in the boundary layers of our domain, because we need only resolve it in one dimension. We solve the radial component of each equation using the open source pseudospectral code Dedalus (Burns et al., in prep). We compute the radial components on a grid of Chebyshev polynomials, as is appropriate for bounded one-dimensional domains (e.g. Boyd 2001). The nonuniform spacing of the Chebyshev grid allows us to resolve the boundary structures well on a 256-point grid. See Figure 3 for an example of the boundary-layer resolution we achieve in a nonlinear term.

We solve the system up to $\mathcal{O}(\epsilon^3)$ in order to close the solution at $\mathcal{O}(\epsilon^2)$.

To find a bounded solution at each order, we eliminate secular terms: terms which are resonant with solutions to the homogenous equation and cause the solution to grow without bound. The elimination of secular terms requires enforcement of solvability criteria, which arise as a consequence of the Fredholm alternative (e.g. Guenther & Lee 1988). The solvability criterion is found by

N_{20}^{Ψ} $N_{20}^{u_y}$ N_{20}^{A} $N_{20}^{B_y}$
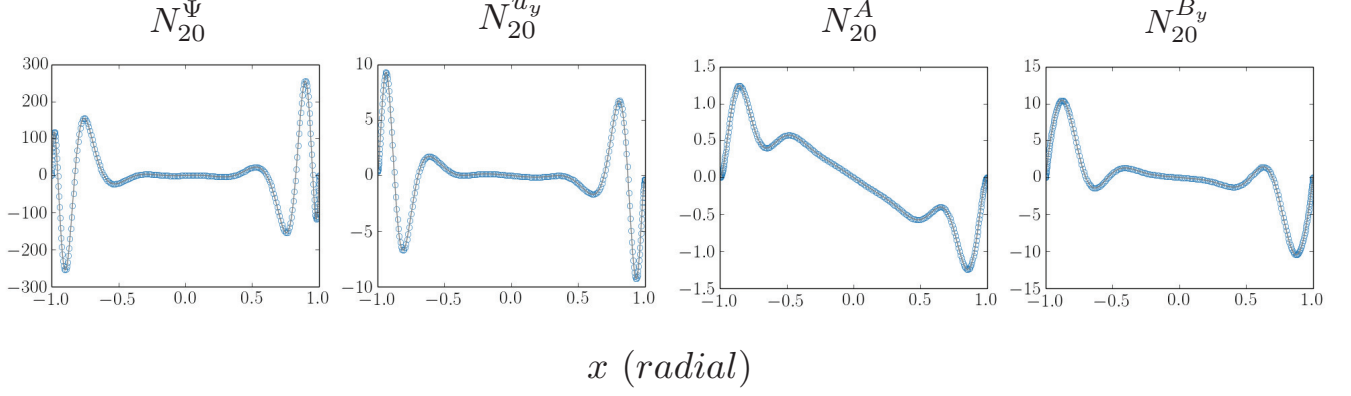
$x \ (radial)$

FIG. 3.— Example of a nonlinear term solved on a 256-point Chebyshev grid. Circles represent values on the Chebyshev grid, grey lines are fits.

forcing the inner product of the equation with its adjoint homogenous solution to be zero. For instance, Equation 36 contains a term $\widetilde{\mathcal{L}}_1 \partial_Z \mathbf{V_1}$ that is resonant with $e^{ik_c z}$. Because the adjoint homogenous equation

$$\mathcal{L}^\dagger \mathbf{V}^\dagger = 0 \qquad (40)$$

has a nontrivial solution, the solvability criterion

$$\left\langle \mathbf{V}^\dagger \cdot \widetilde{\mathcal{L}}_1 \partial_Z \mathbf{V_1} \right\rangle = 0 \qquad (41)$$

must be satisfied in order for Equation 36 to have a solution. In the above,

$$\mathbf{V}^\dagger = \mathbb{V}^\dagger(x) e^{ik_c z} + c.c., \qquad (42)$$

where, again, $\mathbb{V}^\dagger$ contains the radial contribution. The elimination of this inner product must also be enforced on the terms in Equation 37 that are resonant with $e^{ik_c z}$, which are

$$\mathcal{D}\mathbb{V}_{11}e^{iQz}\partial_T \alpha + \alpha \left|\alpha^2\right| \mathbf{N}_{31} e^{iQz} + \alpha \partial_Z \beta \widetilde{\mathbf{N}}_{31} e^{iQz} =$$
$$- \partial_Z^2 \alpha \widetilde{\mathcal{L}}_1 \mathbb{V}_{21} e^{iQz} + \partial_Z^2 \alpha \widetilde{\mathcal{L}}_2 \mathbb{V}_{11} e^{iQz} - \partial_Z \alpha \mathbb{V}_{11} \mathcal{X} e^{iQz}$$
$$+ iQ^3 \alpha \mathcal{L}_3 \mathbb{V}_{11} e^{iQz}. \qquad (43)$$

Taking the inner product yields the amplitude equation

$$a\partial_T \alpha = -c\alpha \left|\alpha^2\right| - \widetilde{c}\alpha\partial_Z\beta - bik_c\alpha + h\partial_Z^2\alpha + gik_c^3\alpha, \qquad (44)$$

where

$$\begin{aligned}
a &\equiv \left\langle \mathbb{V}^\dagger \cdot \mathcal{D}\mathbb{V}_{11}^* \right\rangle \\
c &\equiv \left\langle \mathbb{V}^\dagger \cdot \mathbf{N}_{31}^* \right\rangle \\
\widetilde{c} &\equiv \left\langle \mathbb{V}^\dagger \cdot \widetilde{\mathbf{N}}_{31}^* \right\rangle \\
b &\equiv \left\langle \mathbb{V}^\dagger \cdot (\mathcal{X}\mathbb{V}_{11})^* \right\rangle \\
h &\equiv \left\langle \mathbb{V}^\dagger \cdot \left(\widetilde{\mathcal{L}}_2 \mathbb{V}_{11} - \widetilde{\mathcal{L}}_1 \mathbb{V}_{21} \right)^* \right\rangle \\
g &\equiv \left\langle \mathbb{V}^\dagger \cdot \mathcal{L}_3 \mathbb{V}_{11} \right\rangle,
\end{aligned} \qquad (45)$$

where * denotes a complex conjugate, but $\widetilde{c}$ is equal to zero and drops out of the equation. This is the well-known Ginzburg-Landau equation, and is with only slight modification the same amplitude equation derived in Umurhan et al.

There exists a second amplitude equation, corresponding to the neutral mode, which comes from the solvability condition that must be imposed on all terms in Equation 37 that have no z dependence. These terms are

$$\mathcal{D}\mathbb{U}_{11}\partial_T\beta = \mathcal{L}\mathbf{V_3} + \widetilde{\mathcal{L}}_1 \mathbb{V}_{20} 2 \left|\alpha\right| \partial_Z\alpha - \widetilde{\mathcal{L}}_1 \mathbb{U}_{20} \partial_Z^2\beta$$
$$+ \widetilde{\mathcal{L}}_2 \mathbb{U}_{11} \partial_Z^2\beta - \mathcal{X}\mathbb{U}_{11}\partial_Z\beta, \qquad (46)$$

and taking the inner product of these terms with the adjoint homogenous solution $\mathbb{U}_{11}$ yields

$$\partial_T\beta = k2\left|\alpha\right|\partial_Z\alpha - m\partial_Z^2\beta + \frac{1}{\mathrm{Rm}}\partial_Z^2\beta - p\alpha^*\partial_Z\alpha, \qquad (47)$$

where

$$\begin{aligned}
n &\equiv \left\langle \mathbb{U}_{11} \cdot (\mathcal{L}\mathbb{V}_{30})^* \right\rangle \\
k &\equiv \left\langle \mathbb{U}_{11} \cdot \left(\widetilde{\mathcal{L}}_1 \mathbb{V}_{20} \right)^* \right\rangle \\
m &\equiv \left\langle \mathbb{U}_{11} \cdot \left(\widetilde{\mathcal{L}}_1 \mathbb{U}_{20} \right)^* \right\rangle \\
p &\equiv \left\langle \mathbb{U}_{11} \cdot N_{30}^* \right\rangle,
\end{aligned} \qquad (48)$$

but both k and p are equal to zero. Thus this amplitude equation decouples from Equation 44, and reveals itself to be a simple diffusion equation,

$$\partial_T\beta = -m\partial_Z^2\beta + \frac{1}{\mathrm{Rm}}\partial_Z^2\beta. \qquad (49)$$

Equation 44 is an amplitude equation – a function of the slow variables Z and T. We solve this initial value problem using Dedalus to obtain the asymptotic behavior of α. This is the saturation amplitude. We use the saturation amplitude as α and the radial component of computed on the Chebyshev grid to plot $\mathbf{V}$. We show both first order ($\epsilon \mathbf{V}_1$), second order ($\epsilon^2 \mathbf{V}_2$), and combined first and second order fluid perturbations ($\epsilon \mathbf{V}_1 +$
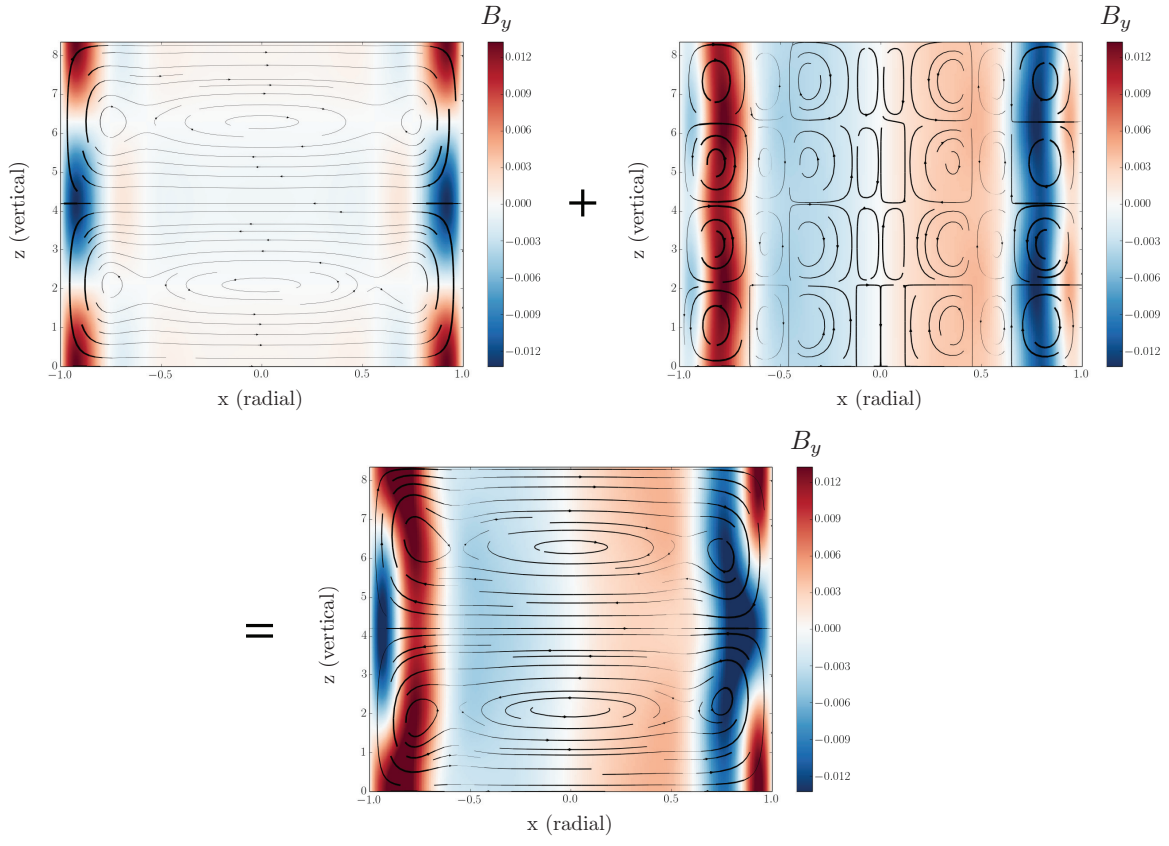
FIG. 4.— First order (left) and second order (right) velocity perturbations. Streamlines represent velocity in the vertical-radial plane, where thicker streamlines correspond to faster speeds. The colorbar represents azimuthal velocity.
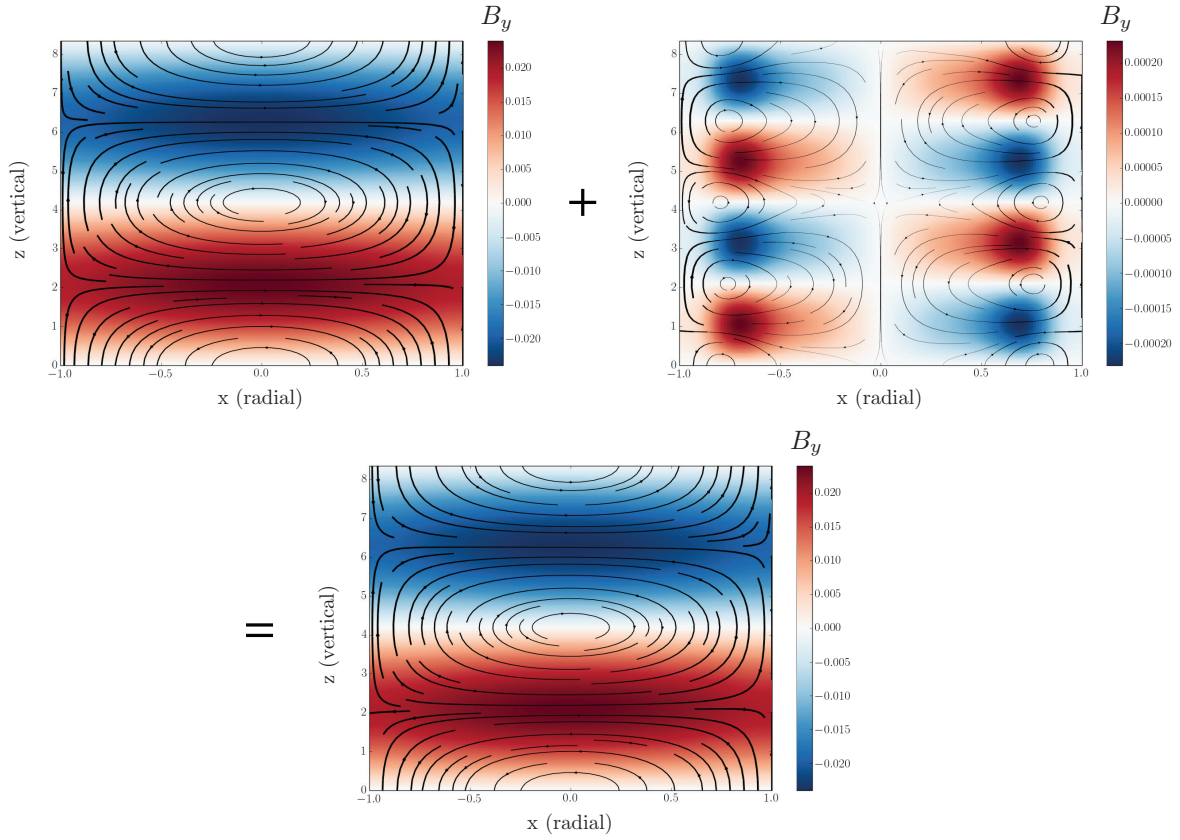

FIG. 5.— First order (left) and second order (right) magnetic field perturbations. Streamlines represent velocity in the vertical-radial plane, where thicker streamlines correspond to higher magnetic field strengths. The colorbar represents azimuthal magnetic field strength.

($\epsilon^2 \mathbf{V}_2$). Figure 4 shows the velocity perturbations, and Figure 5 shows the magnetic field perturbations.

Our analytic formulation is advantageous because we can now analyze the contributions of each fluid quantity at each order. This allows us to directly identify the source of saturation. Equation 44 asymptotically approaches a value, so the system is clearly saturating, and our approach now allows us to quantify the individual contribution of each term. In Figure 4, we see significant fluid action in the second-order velocity plot. By contrast, the second-order magnetic field perturbations are two orders of magnitude smaller than the first-order perturbations (Figure 5). It appears that the second-order velocity perturbations are instrumental in the saturation of the MRI. The likely mechanism is a reduction in the background shear.

4. PARAMETER SPACE

We conduct a full study of the MRI parameter space, focussed on the behavior with changing magnetic Prandtl number ($\text{Pm} \equiv \frac{\text{Rm}}{\text{Re}} \equiv \frac{\nu}{\eta}$). In protoplanetary disks, as well as in liquid metal MRI experiments, the magnetic Prandtl number can be very small ($\text{Pm} \sim 10^{-6}$). The scale separations caused by these large ratios of diffusivity to viscosity render the small Prandtl number regime inaccessible to simulations. This analytic formulation allows us to explore the behavior down to magnetic Prandtl numbers of [TBD!].

5. DISCUSSION

Our domain is designed to be relevant to the design of the Princeton Plasma Physics Laboratory (PPPL) MRI experiment (Ji et al. 2001). A challenge for all MRI experiments is to reduce all extraneous flows which may stabilize the MRI or obscure its detection. In particular, care must be taken to mitigate meridional flows introduced by the endcaps of the experimental apparatus. The PPPL MRI experiment employs a novel design using concentric, differentially rotating rings as endcaps (Schartman et al. 2009). In this investigation, we use periodic vertical boundary conditions, so our set-up represents an idealized domain where endcap contamination does not exist. Future work will address specifically our predictions for the PPPL MRI experiment.

We compute the solutions to our derived equations pseudospectrally, using Dedalus. One advantage to using Dedalus for these computations is that the code can compute the evolution of the fully nonlinear MRI system on the same Fourier/Chebyshev grid. This allows us to directly compare simulation and theory.

This work analyzes Taylor Couette flow in the thin-gap limit, where the channel width is radially narrow compared to its distance from the center of rotation. This simplifies the math by allowing curvature terms to drop out at lowest order. The relaxation of the thin-gap approximation is an obvious next step for this work. The term expansion in the weakly nonlinear analysis will be more formidable in the wide-gap regime, but could prove informative for comparison to experiments.

The present configuration, that of magnetized Taylor Couette flow with a purely axial magnetic field, represents the initial conditions for the standard MRI. The helical MRI is a related, but separate, MHD instability, and was first discovered by Hollerbach and Rüdiger

(2005). It arises in the presence of combined axial and azimuthal fields. To seed helical MRI in our current set-up, we need only add an azimuthal component to our initial background magnetic field. This will be an avenue of future study, and will yield an analytic theory relevant to the above-mentioned PROMISE experiment.

Our results suggest that the primary driver of saturation is reduction of the background shear. We note that while shear modification is relevant in the experimental regime, the gravitational pull of the central body will tend to enforce a Keplerian rotation profile in any astrophysical disk. Thus a modification of the rotation profile is of little relevance as a saturation mechanism to the astrophysical regime. Nevertheless, understanding laboratory MRI experiments is crucial for allowing experimental results to inform our astrophysical understanding of the MRI.

APPENDIX

A. LINEAR DISPERSION RELATION

The linear dispersion relation, which determines the variable scalings in the multiscale analysis.

$$
\begin{aligned}
&\frac{B_0^4 k_x^2 k_z^4}{16\pi^2} + \frac{B_0^4 k_z^6}{16\pi^2} - \frac{B_0^2 \Omega_0 k_z^4 q}{2\pi} - 2\Omega_0 k_z^2 q \sigma^2 - \frac{4\sigma}{\mathrm{Rm}}\Omega_0 k_x^2 k_z^2 q - \frac{4\sigma}{\mathrm{Rm}}\Omega_0 k_z^4 q - \frac{2\Omega_0}{\mathrm{Rm}^2} k_x^4 k_z^2 q - \frac{4\Omega_0}{\mathrm{Rm}^2} k_x^2 k_z^4 q - \frac{2\Omega_0}{\mathrm{Rm}^2} k_z^6 q \\
&- k_x^2 \sigma^4 - k_z^2 \sigma^4 + 4k_z^2 \sigma^2 - \frac{2\sigma^3}{\mathrm{Rm}} k_x^4 - \frac{4\sigma^3}{\mathrm{Rm}} k_x^2 k_z^2 + \frac{8\sigma}{\mathrm{Rm}} k_x^2 k_z^2 - \frac{2\sigma^3}{\mathrm{Rm}} k_z^4 + \frac{8\sigma}{\mathrm{Rm}} k_z^4 - \frac{k_x^6 \sigma^2}{\mathrm{Rm}^2} - \frac{3\sigma^2}{\mathrm{Rm}^2} k_x^4 k_z^2 + \frac{4k_x^4}{\mathrm{Rm}^2} k_z^2 \\
&- \frac{3\sigma^2}{\mathrm{Rm}^2} k_x^2 k_z^4 + \frac{8k_x^2}{\mathrm{Rm}^2} k_z^4 - \frac{k_z^6 \sigma^2}{\mathrm{Rm}^2} + \frac{4k_z^6}{\mathrm{Rm}^2} - \frac{2\sigma^3}{\mathrm{Re}} k_x^4 - \frac{4\sigma^3}{\mathrm{Re}} k_x^2 k_z^2 - \frac{2\sigma^3}{\mathrm{Re}} k_z^4 - \frac{4k_x^6 \sigma^2}{\mathrm{ReRm}} - \frac{12 k_x^4 k_z^2 \sigma^2}{\mathrm{ReRm}} - \frac{12 k_x^2 k_z^4 \sigma^2}{\mathrm{ReRm}} \\
&- \frac{4k_z^6 \sigma^2}{\mathrm{ReRm}} - \frac{2k_x^8 \sigma}{\mathrm{ReRm}^2} - \frac{8k_x^6 k_z^2 \sigma}{\mathrm{ReRm}^2} - \frac{12 k_x^4 k_z^4 \sigma}{\mathrm{ReRm}^2} - \frac{8 k_x^2 k_z^6 \sigma}{\mathrm{ReRm}^2} - \frac{2 k_z^8 \sigma}{\mathrm{ReRm}^2} - \frac{k_x^6 \sigma^2}{\mathrm{Re}^2} - \frac{3\sigma^2}{\mathrm{Re}^2} k_x^4 k_z^2 - \frac{3\sigma^2}{\mathrm{Re}^2} k_x^2 k_z^4 - \frac{k_z^6 \sigma^2}{\mathrm{Re}^2} \\
&- \frac{2 k_x^8 \sigma}{\mathrm{Re}^2 \mathrm{Rm}} - \frac{8 k_x^6 k_z^2 \sigma}{\mathrm{Re}^2 \mathrm{Rm}} - \frac{12 k_x^4 k_z^4 \sigma}{\mathrm{Re}^2 \mathrm{Rm}} - \frac{8 k_x^2 k_z^6 \sigma}{\mathrm{Re}^2 \mathrm{Rm}} - \frac{2 k_z^8 \sigma}{\mathrm{Re}^2 \mathrm{Rm}} - \frac{k_x^{10}}{\mathrm{Re}^2 \mathrm{Rm}^2} - \frac{5 k_x^8 k_z^2}{\mathrm{Re}^2 \mathrm{Rm}^2} - \frac{10 k_x^6 k_z^4}{\mathrm{Re}^2 \mathrm{Rm}^2} - \frac{10 k_x^4 k_z^6}{\mathrm{Re}^2 \mathrm{Rm}^2} \\
&- \frac{5 k_x^2 k_z^8}{\mathrm{Re}^2 \mathrm{Rm}^2} - \frac{k_z^{10}}{\mathrm{Re}^2 \mathrm{Rm}^2} = 0
\end{aligned}
\tag{A1}
$$

B. EXPANSION OF NONLINEAR TERMS

$$
\mathbf{N} = \epsilon^2 \mathbf{N_2} + \epsilon^3 \mathbf{N_3} + \mathcal{O}(\epsilon^4)
\tag{B1}
$$

where

$$
N_2^{(\Psi)} = J(\Psi_1, \nabla^2 \Psi_1) - \frac{2}{\beta} J(A_1, \nabla^2 A_1)
\tag{B2}
$$

$$
N_2^{(u)} = J(\Psi_1, u_1) - \frac{2}{\beta} J(A_1, B_1)
\tag{B3}
$$

$$
N_2^{(A)} = -J(A_1, \Psi_1)
\tag{B4}
$$

$$
N_2^{(B)} = J(\Psi_1, B_1) - J(A_1, u_1)
\tag{B5}
$$

and

$$
\begin{aligned}
N_3^{(\Psi)} = {}&J(\Psi_1, \nabla^2 \Psi_2) - \frac{2}{\beta} J(A_1, \nabla^2 A_2) + J(\Psi_2, \nabla^2 \Psi_1) - \frac{2}{\beta} J(A_2, \nabla^2 A_1) + 2 J(\Psi_1, \partial_z \partial_Z \Psi_1) \\
&- 2\frac{2}{\beta} J(A_1, \partial_z \partial_Z A_1) + \widetilde{J}(\Psi_1, \nabla^2 \Psi_1) - \frac{2}{\beta} \widetilde{J}(A_1, \nabla^2 A_1)
\end{aligned}
\tag{B6}
$$

$$
N_3^{(u)} = J(\Psi_1, u_2) + J(\Psi_2, u_1) + \widetilde{J}(\Psi_1, u_1) - \frac{2}{\beta} J(A_1, B_2) - \frac{2}{\beta} J(A_2, B_1) - \frac{2}{\beta} \widetilde{J}(A_1, B_1)
\tag{B7}
$$

$$
N_3^{(A)} = -J(A_1, \Psi_2) - J(A_2, \Psi_1) - \widetilde{J}(A_1, \Psi_1)
\tag{B8}
$$

$$
N_3^{(B)} = J(\Psi_1, B_2) + J(\Psi_2, B_1) + \widetilde{J}(\Psi_1, B_1) - J(A_1, u_2) - J(A_2, u_1) - \widetilde{J}(A_1, u_1).
\tag{B9}
$$

$\mathbf{N_2}$ and $\mathbf{N_3}$ expand to become

$$
\mathbf{N_2} = \alpha^2 \mathbb{N}_{22} e^{i2k_c z} + |\alpha|^2 \mathbb{N}_{20} + c.c.
\tag{B10}
$$

and

$$
\mathbf{N_3} = \alpha^3 \mathbb{N}_{33} e^{i3k_c z} + \alpha \partial_Z \alpha \mathbb{N}_{32} e^{i2k_c z} + \alpha |\alpha|^2 \mathbb{N}_{31} e^{ik_c z} + \alpha \partial_Z \beta \widetilde{\mathbb{N}}_{31} e^{ik_c z} + \alpha^* \partial_Z \alpha \mathbb{N}_{30} + c.c.
\tag{B11}
$$

The second order nonlinear terms are

$$
\begin{aligned}
N_{22}^{(\Psi)} = {} & ik_c\Psi_{11} \cdot \left(\partial_x^3\Psi_{11} - k_c^2\partial_x\Psi_{11}\right) - \partial_x\Psi_{11} \cdot \left(ik_c\partial_x^2\Psi_{11} - ik_c^3\Psi_{11}\right) \\
& + \frac{2}{\beta}\partial_xA_{11} \cdot \left(ik_c\partial_x^2A_{11} - ik_c^3A_{11}\right) - \frac{2}{\beta}ik_cA_{11} \cdot \left(\partial_x^3A_{11} - k_c^2\partial_xA_{11}\right)
\end{aligned}
\tag{B12}
$$

$$
N_{22}^{(u)} = ik_c\Psi_{11} \cdot \partial_xu_{11} - \partial_x\Psi_{11} \cdot ik_cu_{11} - \frac{2}{\beta}ik_cA_{11} \cdot \partial_xB_{11} + \frac{2}{\beta}\partial_xA_{11} \cdot ik_cB_{11}
\tag{B13}
$$

$$
N_{22}^{(A)} = -ik_cA_{11} \cdot \partial_x\Psi_{11} + \partial_xA_{11} \cdot ik_c\Psi_{11}
\tag{B14}
$$

$$
N_{22}^{(B)} = ik_c\Psi_{11} \cdot \partial_xB_{11} - \partial_x\Psi_{11} \cdot ik_cB_{11} - ik_cA_{11} \cdot \partial_xu_{11} + \partial_xA_{11} \cdot ik_cu_{11}
\tag{B15}
$$

$$
\begin{aligned}
N_{20}^{(\Psi)} = {} & ik_c\Psi_{11} \cdot \left(\partial_x^3\Psi_{11}^* - k_c^2\partial_x\Psi_{11}^*\right) - \partial_x\Psi_{11} \cdot \left(ik_c\partial_x^2\Psi_{11}^* - ik_c^3\Psi_{11}^*\right) \\
& \frac{2}{\beta}\partial_xA_{11} \cdot \left(ik_c\partial_x^2A_{11}^* - ik_c^3A_{11}^*\right) - \frac{2}{\beta}ik_cA_{11} \cdot \left(\partial_x^3A_{11}^* - k_c^2\partial_xA_{11}^*\right)
\end{aligned}
\tag{B16}
$$

$$
N_{20}^{(u)} = ik_c\Psi_{11} \cdot \partial_xu_{11}^* - \partial_x\Psi_{11} \cdot ik_cu_{11}^* - \frac{2}{\beta}ik_cA_{11} \cdot \partial_xB_{11}^* + \frac{2}{\beta}\partial_xA_{11} \cdot ik_cB_{11}^*
\tag{B17}
$$

$$
N_{20}^{(A)} = -ik_cA_{11} \cdot \partial_x\Psi_{11}^* - \partial_xA_{11} \cdot ik_c\Psi_{11}^*
\tag{B18}
$$

$$
N_{20}^{(B)} = ik_c\Psi_{11} \cdot \partial_xB_{11}^* - \partial_x\Psi_{11} \cdot ik_cB_{11}^* - ik_cA_{11} \cdot \partial_xu_{11}^* + \partial_xA_{11} \cdot ik_cu_{11}^*
\tag{B19}
$$

and the third order nonlinear terms become

$$
\begin{aligned}
N_{31}^{(\Psi)} = {} & ik_c\left(\Psi_{11} \cdot \partial_x^3\Psi_{20}\right) + ik_c\left(\Psi_{11} \cdot \partial_x^3\Psi_{20}^*\right) - ik_c\left(\Psi_{11}^* \cdot \partial_x^3\Psi_{22}\right) - i2k_c\left(\partial_x\Psi_{11}^* \cdot \partial_x^2\Psi_{22}\right) \\
& + i8k_c^3\left(\partial_x\Psi_{11}^* \cdot \Psi_{22}\right) + i4k_c^3\left(\Psi_{11}^* \cdot \partial_x\Psi_{22}\right) + \frac{2}{\beta}\left[-ik_c\left(A_{11} \cdot \partial^3A_{20}\right) - ik_c\left(A_{11} \cdot \partial_x^3A_{20}^*\right)\right] \\
& + \frac{2}{\beta}\left[ik_c\left(A_{11}^* \cdot \partial_x^3A_{22}\right) + i2k_c\left(\partial_xA_{11}^* \cdot \partial_x^2A_{22}\right) - i8k_c^3\left(\partial_xA_{11}^* \cdot A_{22}\right) - i4k_c^3\left(A_{11}^* \cdot \partial_xA_{22}\right)\right] \\
& + i2k_c\left(\Psi_{22} \cdot \partial_x^3\Psi_{11}^*\right) - i2k_c^3\left(\Psi_{22} \cdot \partial_x\Psi_{11}^*\right) - ik_c\left(\partial_x\Psi_{20} \cdot \partial_x^2\Psi_{11}\right) + ik_c\left(\partial_x\Psi_{22} \cdot \partial_x^2\Psi_{11}^*\right) \\
& - ik_c\left(\partial_x\Psi_{20}^* \cdot \partial_x^2\Psi_{11}\right) + ik_c^3\left(\partial_x\Psi_{20} \cdot \Psi_{11}\right) + ik_c^3\left(\partial_x\Psi_{20}^* \cdot \Psi_{11}\right) - ik_c^3\left(\partial_x\Psi_{22} \cdot \Psi_{11}^*\right) \\
& + \frac{2}{\beta}\left[-i2k_c\left(A_{22} \cdot \partial_x^3A_{11}^*\right) + i2k_c^3\left(A_{22} \cdot \partial_xA_{11}^*\right) + ik_c\left(\partial_xA_{20} \cdot \partial_x^2A_{11}\right) - ik_c\left(\partial_xA_{22} \cdot \partial_x^2A_{11}^*\right)\right] \\
& + \frac{2}{\beta}\left[ik_c\left(\partial_xA_{20}^* \cdot \partial_x^2A_{11}\right) - ik_c^3\left(\partial_xA_{20} \cdot A_{11}\right) - ik_c^3\left(\partial_xA_{20}^* \cdot A_{11}\right) + ik_c^3\left(\partial_xA_{22} \cdot A_{11}^*\right)\right]
\end{aligned}
\tag{B20}
$$

$$
\begin{aligned}
N_{31}^{(u)} = {} & ik_c\left(\Psi_{11} \cdot \partial_xu_{20}\right) + ik_c\left(\Psi_{11} \cdot \partial_xu_{20}^*\right) - ik_c\left(\Psi_{11}^* \cdot \partial_xu_{22}\right) - i2k_c\left(\partial_x\Psi_{11}^* \cdot u_{22}\right) \\
& - ik_c\left(u_{11} \cdot \partial_x\Psi_{20}\right) - ik_c\left(u_{11} \cdot \partial_x\Psi_{20}^*\right) + ik_c\left(u_{11}^* \cdot \partial_x\Psi_{22}\right) + i2k_c\left(\partial_xu_{11}^* \cdot \Psi_{22}\right) \\
& + \frac{2}{\beta}\left[-ik_c\left(A_{11} \cdot \partial_xB_{20}\right) - ik_c\left(A_{11} \cdot \partial_xB_{20}^*\right) + ik_c\left(A_{11}^* \cdot \partial_xB_{22}\right) + i2k_c\left(\partial_xA_{11}^* \cdot B_{22}\right)\right] \\
& + \frac{2}{\beta}\left[ik_c\left(B_{11} \cdot \partial_xA_{20}\right) + ik_c\left(B_{11} \cdot \partial_xA_{20}^*\right) - ik_c\left(B_{11}^* \cdot \partial_xA_{20}\right) - i2k_c\left(\partial_xB_{11}^* \cdot A_{22}\right)\right]
\end{aligned}
\tag{B21}
$$

$$
\begin{aligned}
N_{31}^{(A)} = {} & -ik_c\left(A_{11} \cdot \partial_x\Psi_{20}\right) - ik_c\left(A_{11} \cdot \partial_x\Psi_{20}^*\right) + ik_c\left(A_{11}^* \cdot \partial_x\Psi_{22}\right) + i2k_c\left(\partial_xA_{11}^* \cdot \Psi_{22}\right) \\
& + ik_c\left(\Psi_{11} \cdot \partial_xA_{20}\right) + ik_c\left(\Psi_{11} \cdot \partial_xA_{20}^*\right) - ik_c\left(\Psi_{11}^* \cdot \partial_xA_{22}\right) - i2k_c\left(\partial_x\Psi_{11}^* \cdot A_{22}\right)
\end{aligned}
\tag{B22}
$$

$$
\begin{aligned}
N_{31}^{(B)} =\ & ik_c \left(\Psi_{11} \cdot \partial_x B_{20}\right) + ik_c \left(\Psi_{11} \cdot \partial_x B_{20}^*\right) - ik_c \left(\Psi_{11}^* \cdot \partial_x B_{22}\right) - i2k_c \left(\partial_x \Psi_{11}^* \cdot B_{22}\right) \\
& - ik_c \left(B_{11} \cdot \partial_x \Psi_{20}\right) - ik_c \left(B_{11} \cdot \partial_x \Psi_{20}^*\right) + ik_c \left(B_{11}^* \cdot \partial_x \Psi_{22}\right) + i2k_c \left(\partial_x B_{11}^* \cdot \Psi_{22}\right) \\
& - ik_c \left(A_{11} \cdot \partial_x u_{20}\right) - ik_c \left(A_{11} \cdot \partial_x u_{20}^*\right) + ik_c \left(A_{11}^* \cdot \partial_x u_{22}\right) + i2k_c \left(\partial_x A_{11}^* \cdot u_{22}\right) \\
& ik_c \left(u_{11} \cdot \partial_x A_{20}\right) + ik_c \left(u_{11} \cdot \partial_x A_{20}^*\right) - ik_c \left(u_{11}^* \cdot \partial_x A_{22}\right) - i2k_c \left(\partial_x u_{11}^* \cdot A_{22}\right)
\end{aligned}
\tag{B23}
$$

REFERENCES

Balbus, S A and Hawley, J F, 1991, The Astrophysical Journal, 376, 214

Boyd, J P, 2001, Chebyshev and Fourier Spectral Methods, New York, Dover

Chandrasekhar, S. 1960, Proceedings of the National Academy of Sciences of the United States of America, 46, 253

Cooper, C M, Wallace, J, Brookhart, M, Clark, M, Collins, C, Ding, W X, Flanagan, K, Khalzov, I, Li, Y, Milhone, J, Nornberg, M, Nonn, P, Weisberg, D, Whyte, D G, Zweibel, E, Forest, C B, Physics of Plasmas, 2013, 21, 013505

Gissinger, C, Ji, H, Goodman, J, Phys. Rev. E, 2011, 84, 026308

Goodman, J, Xu, G, 1994, ApJ, 432, 213

Hollerbach, R, Proc. R. Soc. A, 2009, 465, 2107

Hollerbach, R, Rdiger, G, Phys. Rev. Lett, 2005, 95, 124501

Ji, H, Goodman, J, Kageyama, A, Mon. Not. R. Astron. Soc., 2001, 325, 1

Knobloch, E, Julien K, 2005, Physics of Fluids, 17, 094106

Pessah, M, 2010, ApJ, 716, 1012

Schartman, E, Ji, H, Burin, M J, Rev Sci Instrum, 2009, 80, 024501

Shakura, N I and Sunyaev, R A, Astronomy & Astrophysics, 1973, 24, 337

Sisan, D R, Mujica, N, Tillotson, W A, Huang Y-M, Dorland, W, Hassam, A B, Antonsen, T M, Lathrop, D P, Phys Rev Lett, 2004, 93, 11

Stefani, F, Gundrum, T, Gerbeth, G, Rdiger, G, Schultz, M, Szklarski, J, Hollerbach, R, Phys Rev Lett, 2006, 97, 184502

Umurhan, O M, Regev, O, Menou, K, 2007, Phys. Rev. Letters, 98, 034501

Umurhan, O M, Regev, O, Menou, K, 2007, Phys. Rev. E, 76, 036310